RSC Advances

PAPER

View Article Online
View Journal | View Issue

Cite this: *RSC Adv.*, 2024, **14**, 9587

Synthesis of urchin-like $NiCo_2S_4$ electrode materials based on a two-step hydrothermal method for high-capacitance supercapacitors

Jingyu Tian, Jingjia Zhang and Xiaofeng Li *

Received 14th January 2024
Accepted 7th March 2024

DOI: 10.1039/d4ra00361f

rsc.li/rsc-advances

Transition metal sulfides have been considered as promising electrode materials for future super-capacitors due to their spinel structures and environmentally friendly properties. Among these materials, $NiCo_2S_4$ compounds exhibit high theoretical specific capacity but poor cycling performance. To address this issue, we synthesize several $NiCo_2S_4$ urchin balls. The NCS-1.5 nanospheres demonstrate a specific capacitance of 1352.2 F g^{-1} at a current density of 1 A g^{-1}, and maintain high specific capacity after 10 000 charge–discharge cycles. An asymmetric capacitor assembled with the NCS-1.5 sample as the cathode and activated carbon as the anode achieve an energy density of 45.5 W h kg^{-1} at 2025 W kg^{-1}. The urchin-like nanospheres also facilitate the combination with other materials, providing potential insights for the synthesis of supercapacitor electrode materials.

Introduction

Due to the rapid advancement of industry and technology, the demand for energy is steadily increasing. Conventional fossil fuels are finite resources and detrimental to the ecological environment. Hence, it is imperative to devise and create sustainable green energy sources.[1–3] There are different types of energy storage devices such as capacitors, supercapacitors, batteries and fuel cells.[4–7] Super-capacitors attract much attention from researchers due to their high-power density, and cycle stability.[8–10] The current research focus on supercapacitors is on enhancing their energy density while ensuring high-power and cycle stability.[11–13] Increasing the specific capacitance and expanding the voltage window are two important methods to enhance energy density.[14]

Currently, the majority of research is concentrated on developing new materials to enhance specific capacitance. Among these, transition metal sulfides exhibit numerous valence states and undergo plentiful redox reactions.[15] In particular, ternary transition metal sulfides (such as $NiCo_2S_4$,[16] $FeCo_2S_4$,[17] $MnCo_2S_4$,[18] and $ZnCo_2S_4$,[19] *etc.*) have been investigated intensively due to their high theoretical capacitance, low toxicities and costs. Recently, $NiCo_2S_4$ with spinel structure have drawn more attention. In AB_2S_4 spinel structure, sulfur ions as cubic close-packed, where A ions (Ni^{2+}, Co^{2+}) fill in the tetrahedral voids and B ions (Co^{3+}) in the octahedral voids.[20,21] In addition, $NiCo_2S_4$ materials possess multiple forms to improve ion diffusion. For example, Pu *et al.* prepare $NiCo_2S_4$ nanotube arrays with a specific capacitance of 738 F g^{-1} at 4 A g^{-1}.[22] Hussain S synthesizes zero-dimensional 14-sided (6 squares and 8 rectangles) $NiCo_2S_4$ cubic hexa-octahedral (NCS–COH) using a simple hydrothermal route.[23] Xie's group use an one-pot method to compose spinel-type $NiCo_2S_4$ nanoparticles/carbon nanotubes (CNT).[24] Preparation of $NiCo_2S_4$ layered nanostructures by microwave-assisted hydrothermal/solvothermal strategy by Li.[25]

In this study, we utilize a two-step hydrothermal method to fabricate urchin-shaped nanospheres of $NiCo_2S_4$. The resulting samples exhibit a specific capacity of 1352 F g^{-1} at 1 A g^{-1}. Furthermore, the capacitance retention remains at 87.82% after 10 000 cycles. Assembling an asymmetric capacitor with NCS-1.5 NF as the cathode and activated carbon as the anode resulted in a high energy density of 45.5 W h kg^{-1} at 2025 W kg^{-1}.

Results and discussion

Fig. 1 illustrates $NiCo_2S_4$ materials synthesis pathway. $NiCo_2S_4$ urchin-like nanospheres are grown on a nickel foam substrate by two-step hydrothermal method. The composition and crystal

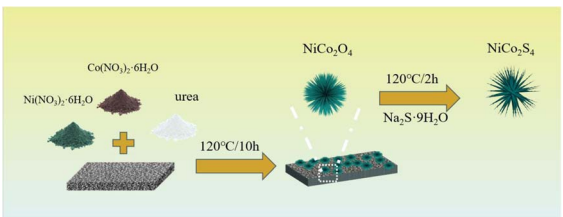

Fig. 1 Synthetic schematic of the $NiCo_2S_4$ urchin-like structure.

College of Chemical and Chemistry, Harbin Normal University, Harbin 150025, P. R. China

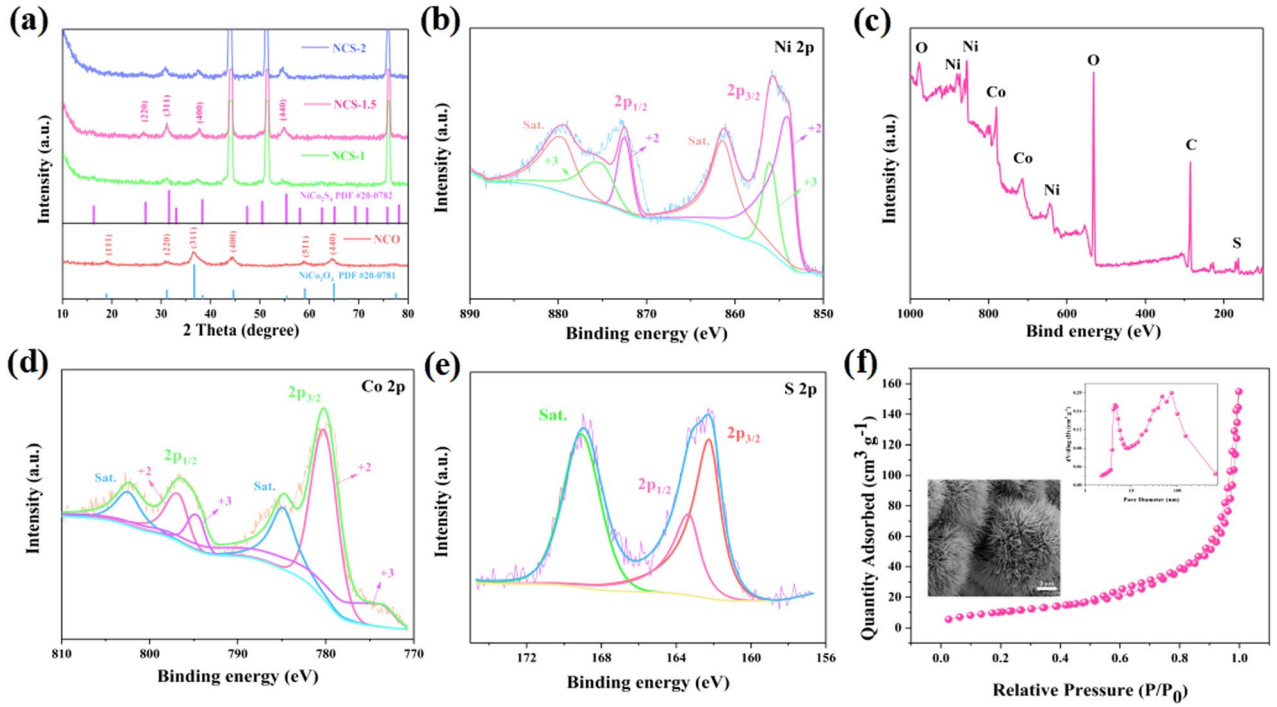

Fig. 2 Structural characterization (a) XRD patterns (b) XPS survey spectra (c) Ni 2p (d) Co 2p (e) S 2p (f) N_2 adsorption–desorption isotherms (the insets present the pore size distribution curves and SEM image of the $NiCo_2S_4$ nanosheets).

structure of the four samples are first analyzed by XRD spectroscopy. As shown in Fig. 2a, the diffraction peaks at 18.91, 31.15, 36.70, 44.62, 59.09, and 64.98° correspond to the (111), (220), (311), (400), (511), and (440) crystal planes of $NiCo_2O_4$, phase (JCPDS no. 20-0781) respectively. After the addition of $Na_2S{\cdot}9H_2O$, the peaks at 26.83, 31.59, 38.32, and 55.33° correspond to the (220), (311), (400), and (440) crystal planes of the $NiCo_2S_4$ respectively. The XRD spectra of the samples do not change for different $Na_2S{\cdot}9H_2O$ contents. It illustrates that impurities are also not generated in the product.

We use XPS to recognize the surface elemental composition and valence of $NiCo_2S_4$ samples. Fig. 2b presents the survey spectra of $NiCo_2S_4$ materials. The peaks correspond to the Ni, Co, S, and O elements. Elemental O come from CO_2 absorbed in the air or from a small amount of oxidation of the sample.[26] The Ni 2p and Co 2p of XPS spectra be well fitted with two spin–orbit doublets and two shakeup satellites (marked as "Sat."). As shown in Fig. 2c, the peaks at 855.7 and 872.4 eV correspond to Ni $2p_{3/2}$ and Ni $2p_{1/2}$, respectively. The difference of binding energy between Ni $2p_{3/2}$ and Ni $2p_{1/2}$ is 16.7 eV, indicating the coexistence of Ni^{2+} and Ni^{3+}.[27] Fig. 2d, depicts the Co 2p XPS spectrum. The peaks at 779.3 and 795.6 eV are related to Co $2p_{3/2}$ and Co $2p_{1/2}$, respectively, suggesting the coexistence of Co^{2+} and Co^{3+}.[28] The S 2p spectrum (Fig. 2e) is divided into two main peaks and one shake-up satellite. The component at 163.4 eV is typical of metal–sulfur bonds,[29] while the peak at 162.2 eV can be attributed to the sulfur ion in low coordination at the surface. The XPS spectra closely match the theoretical composition of the $NiCo_2S_4$ material. Fig. 2f shows the nitrogen adsorption desorption isotherm of the NCS-1.5 sample. The inset presents the pore size distribution and SEM image of NCS materials. The specific surface area of NCS samples is 35.311 m^2 g^{-1}. The samples show an urchin-like distribution. The large specific surface area and the porous structure increase the contact area with the electrolyte, which accelerates the ion transport.[30]

Then we use scanning electron microscopy (SEM) to observe the sample morphology. Fig. 3a and e present that the NCO samples are composed of nano-needles arrange closely in rows and the surface of the nano-needles is smooth. As shown in Fig. 3b and f, after vulcanization with 1.5 mmol $Na_2S{\cdot}9H_2O$, the surface of NCS-1.5 nano pins become rough compared to NCO nano pins. This is attributed to the substitution of oxygen by sulfur during recrystallisation during vulcanization, resulting in the formation of nanocrystalline particles.[19] This configuration reveals empty spaces and creates a permeable framework. It enhances the interaction area with the electrolyte and eases ion transportation.[31] Transitional vulcanization changes the morphology of the samples in Fig. 3d and h. The transformation of nano-needles into nanosheets and subsequent layer stacking results in suboptimal electrochemical performance.[32] The element mappings (Fig. 3i–l) also indicate that the composite material consists of S, Co, Ni.

The electrochemical performances of the samples are evaluated using a three-electrode system in 3 M KOH electrolyte. Fig. 4a presents the CV curves of the electrodes at 100 mV s^{-1}. Clearly, NCS-1.5 material shows higher peak current density and larger closed CV curve area. Suggesting that the NCS-1.5 electrode has larger charge storage capacity.[33] In Fig. 4d, distinct redox peaks appear at different scanning speeds. These

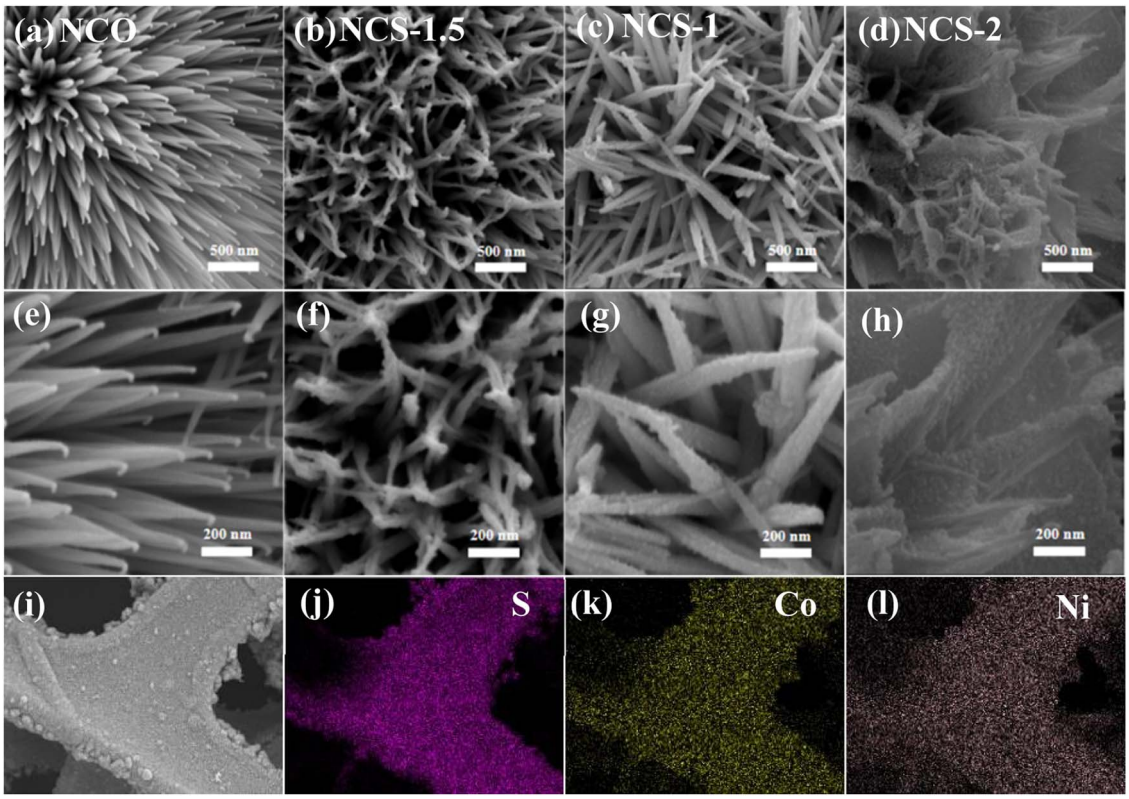

Fig. 3 Morphology characterization (a–d) low-magnification SEM images (e–h) high-magnification SEM images (i–l) element mappings. SEM, scanning electron microscope.

distinct peaks can be attributed to the reversible faradaic redox processes of $Co^{2+}/Co^{3+}/Co^{4+}$ and Ni^{2+}/Ni^{3+} based on the following reactions:[11]

$$CoS + OH^- \rightleftarrows CoSOH + e^- \quad (1)$$

$$CoSOH + OH^- \rightleftarrows CoSO + H_2O + e^- \quad (2)$$

$$NiS + OH^- \rightleftarrows NiSOH + e^- \quad (3)$$

In addition, the first pair of redox peaks in CV curves is related to faradaic reactions of $NiCo_2S_4$ to form NiSOH and CoSOH. Whereas, the second pair of peaks is due to the redox reaction between CoSOH and CoSO.[34]

According to the GCD curve (Fig. 4b) of current density at 1 A g^{-1}, the NCS-1.5 sample has the longest charge–discharge time of 1600 s. It is proved that NCS-1.5 material has the largest specific capacitance. Fig. 4e presents the GCD curves of NCS-1.5 product at the current density range of 1–8 A g^{-1}. The non-triangular shapes with obvious plateaus further confirm the battery-like behavior of the electrodes. And no significant iR drop is observed at low current densities, indicating that the NCS-1.5 electrode has good conductivity.[33,35]

EIS is also an important parameter to determine the electrochemical properties of the electrode material in Fig. 4c. R_S represents the internal resistance between the electrolyte and the electrode. The R_S values for NCO, NCS-1, NCS-1.5, and NCS-2 are 0.52 Ω, 0.59 Ω, 0.56 Ω, 0.60 Ω, respectively. R_{ct} is the charge transfer resistance. In the high-frequency region, the NCO sample possesses a complete semicircle, indicating a large charge transfer resistance. W refers to the ion diffusion resistance, in the low-frequency region, the NCS-1.5 sample possesses a large slope proving its strong ionic diffusion. Fig. 4f shows the specific capacitance of the sample at different current densities. The specific capacitance of NCS-1.5 electrode is 1352.2 F g^{-1} at a current density of 1 A g^{-1}, which is superior to other samples. The capacitive behavior of the sample during charging and discharging can be obtained according to the following equation:

$$I = av^b \quad (4)$$

v refers to the scanning speed, and a and b are constants. The surface controls play a dominated role when b is less than 0.5. The reaction is controlled by diffusion behaviors when b is equal (more) to 1.[36] The slope falls within the range of 0.5–1 as depicted in Fig. 4g. The electrode material exhibits the simultaneous presence of surface control behavior and diffusion control behavior. The capacitance of the sample is mainly provided by diffusion capacitance and surface capacitance. At high sweeping speeds, the timeliness of ion diffusion decreases, causing the surface control's contribution to gradually increase, as depicted in Fig. 4h.[37] The contribution rate of surface control and diffusion control can be evaluated by the following formula:

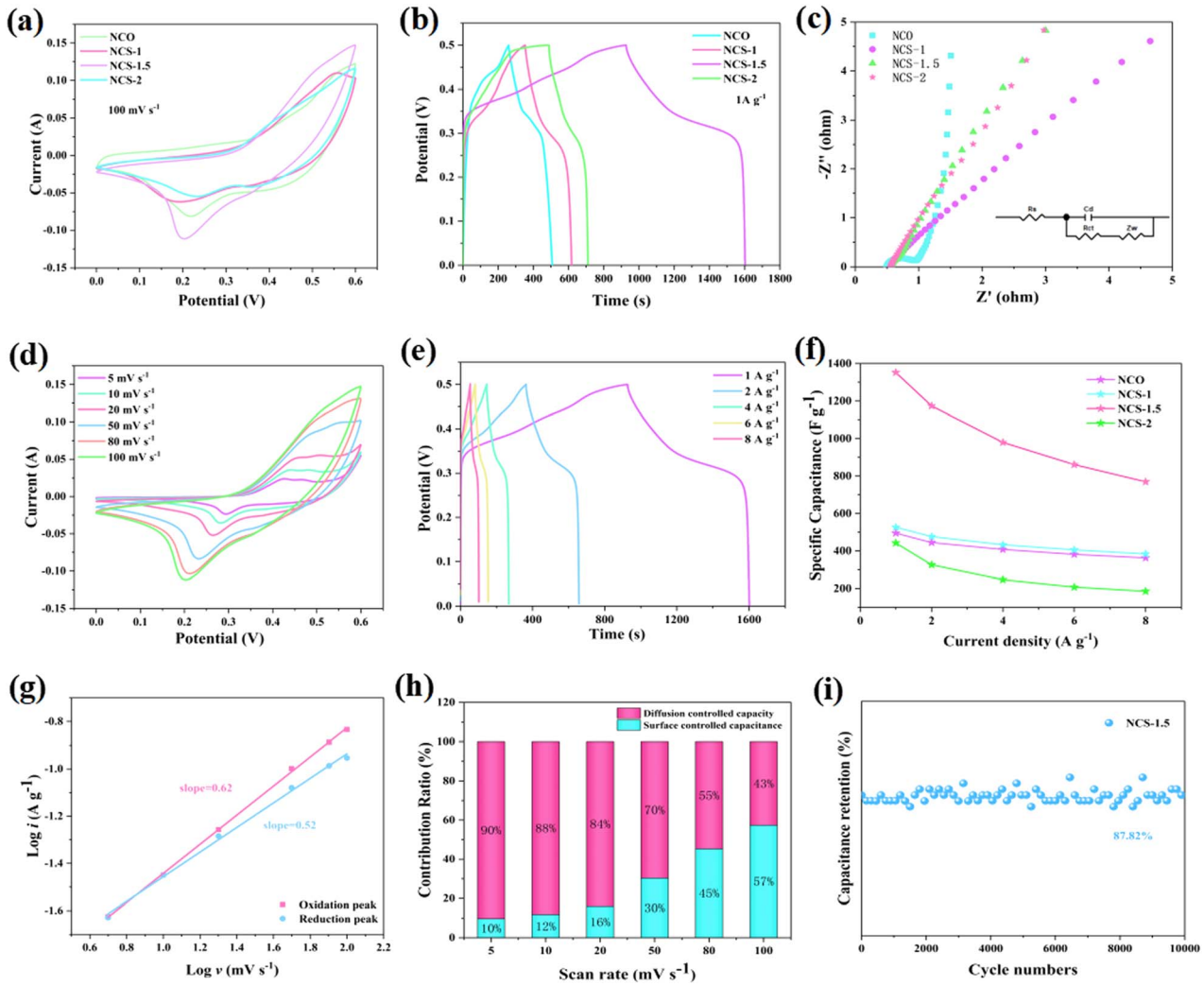

Fig. 4 Electrochemical performance (a) CV curves (b) GCD curves (c) Nyquist plots (d) the CV curves of NCS-1.5 sample (e) the GCD curves of NCS-1.5 sample (f) specific capacitance (g) b values of NCS-1.5 (h) contribution rate of surface-controlled capacitance and diffusion-controlled capacity (i) cycling stability.

$$i(v) = k_1 v + k_2 v^{1/2} \quad (5)$$

The values of k_1 and k_2 in the equation can be calculated by CV curves. In addition, the cycling performance of the sample is critical. As shown in Fig. 4i the retention rate of NCS-1.5 samples after 10 000 charge–discharge cycles still reach 87.82%. It reflects the outstanding cycling performance of the sample.

To investigate the application of the samples, we assemble a hybrid capacitor using an NCS-1.5 electrode as the cathode and an AC as the anode. The CV window of activated carbon is 0–1. Fig. 5a shows that the device reaches 1.6 V at a scanning rate of 20 mv s^{-1}. The CV curves remain rectangular shape at the different scan rates and different voltage windows in Fig. 5b and c. It indicates a high electrochemical stability and capacitance.[38] The device is discharged for 91 s at a current density of 0.5 A g^{-1} (Fig. 5d). From the EIS, the R_S value of the device is 2.36 Ω (Fig. 5e). As shown in Fig. 5f, the capacitance retention of NCS-1.5//AC is 81.98% after 10 000 cycles of charging and discharging. It demonstrates the desirable cycling stability and application of the device. At the same time, LED bulb is successfully lit *via* the three devices in series (inset of Fig. 5f). The energy density of NCS-1.5//AC at 2025 W kg^{-1} is calculated to be 45.5 W h kg^{-1}, which is higher than that of the previously reported devices as shown in Table 1.

Experimental section

All the reagents utilized in the experiment are of analytical purity. Prior to the synthesis of the material, a 3 × 4 cm^2 piece of nickel foam was subjected to repeated washings with ethanol and deionized water. Then, 2 mmol of $Ni(NO_3)_2 \cdot 6H_2O$, 2 mmol of $Co(NO_3)_2 \cdot 6H_2O$, 9 mmol of urea were dissolved into 60 mL of deionized water and stirred for 30 min. Next, the pre-treated nickel foam and the aforementioned solution were transferred into a 100 mL PTFE lined autoclave and maintained at 120 °C for 10 hours. After being cooled to room temperature, the nickel foam was rinsed several times with deionized water and

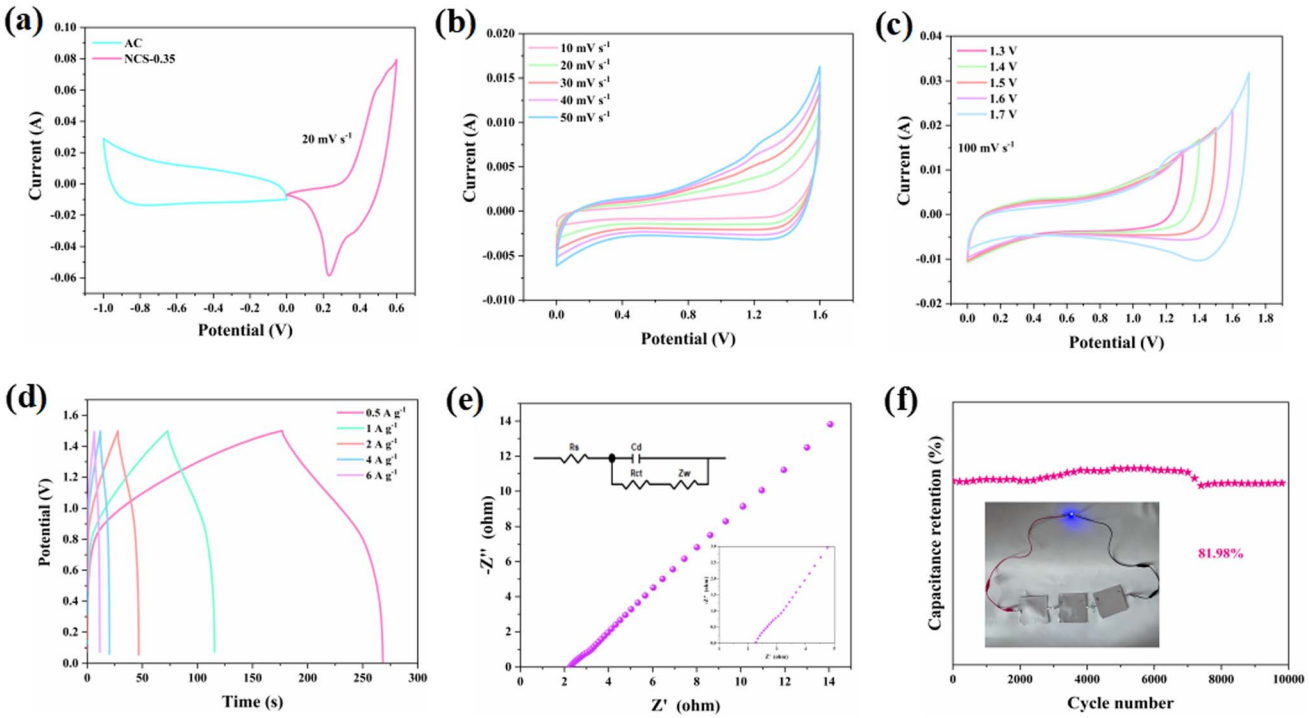

Fig. 5 Electrochemical performance of asymmetric device (a) the CV curves of NCS-1.5 and AC (b and c) CV curves with different scan rates and voltage windows (d) GCD curves (e) Nyquist plots (f) cycling performance (inset photograph of lighting LED).

Table 1 The energy densities and power densities of several devices

Electrode materials	Specific capacity	Cyclic performance	Energy density	Power density	Ref.
NCS/NF//N-RGONS/NF	987.2 C g^{-1} (2 A g^{-1})	83.9% (8000 times after)	67.5	850	39
Ni–Co–S/NF//AC	1406.9 F g^{-1} (0.5 A g^{-1})	88.6% (1000 times after)	24.8	849.5	40
$NiCo_2S_4$@NiO//AC	12.2 F cm^{-2} (1 mA cm^{-2})	88.8% (10 000 times after)	30.38	288	41
$NiCo_2S_4$@NiS//AC	1314 C g^{-1} (1 A g^{-1})	96.2% (5000 times after)	62.4	800	42
$NiCo_2S_4$/NCF//OMC/NCF	1231 F g^{-1} (2 A g^{-1})	90.4% (2000 times after)	45.5	512	43
$NiCo_2S_4$//AC	1352.2 F g^{-1} (1 A g^{-1})	87.82% (10 000 times after)	45.5	2025	This work

ethanol, and then subjected to a heat treatment at 350 °C for 2 hours. Finally, 1.5 mmol of $Na_2S{\cdot}9H_2O$ with 60 mL of deionized water and the above precursors was put into an autoclave at 120 °C for 2 h. The nickel foam washed several times and dried for 4 h, named NCS-1.5. The average mass loading was 1.3 mg cm^{-2}. For comparison, without $Na_2S{\cdot}9H_2O$, with 1 mmol of $Na_2S{\cdot}9H_2O$, and with 2 mmol of $Na_2S{\cdot}9H_2O$ were synthesized in the above pathways and named NCO, NCS-1, and NCS-2. The whole formation process is given in the following equation:

$$Ni^{2+} + 2Co^{2+} + 6OH^- \rightarrow NiCo_2(OH)_6 \quad (6)$$

$$NiCo_2(OH)_6 + 1/2O_2 \rightarrow NiCo_2O_4 + 3H_2O \quad (7)$$

$$NiCo_2O_4 + S^{2-} \rightarrow NiCo_2S_4 + O^{2-} \quad (8)$$

The samples were initially analysed for composition using a powder X-ray diffraction analyser (XRD, Shimadzu-7000). We observed the morphology and microstructure of the samples using a scanning electron microscope (SEM, Gemini 300-71-31). The elemental and valence states of the samples were analysed by X-ray photoelectron spectroscopy (XPS, Thermo Scientific K-Alpha). Finally, we used Bruner–Emmett–Taylor (BET) to calculate the specific surface area and pore size of the samples.

The electrochemical experiments of the samples were performed using an electrochemical workstation (Shanghai Chenhua, CHI660E). The prepared materials were used as the working electrode, Hg/HgO as the reference electrode and Pt foil as the counter electrode. Several devices were assembled to further explore the practicality of the samples. NCS-1.5 samples were used as the positive electrodes, AC as the negative electrode, and PVA/KOH gel as electrolyte. The mass ratio of activated carbon, carbon black and polyvinylidene fluoride (PVDF) was 7 : 2 : 1. *N*-Methyl-2-pyrrolidone was then added dropwise until a homogeneous slurry was obtained. It was coated on nickel foam and dried. According to the charge balance principle of an electrode material ($q^+ = q^-$), the following formulas are abided by:[44]

$$Q = It = Cm\Delta V \quad (9)$$

$$m^+/m^- = Cm^-(\Delta V)^-/Cm^+(\Delta V)^+ \quad (10)$$

where Q, I, t, C, m, and ΔV denote the charge storage capacity, discharge current, discharge time, specific capacitance, mass of the materials and voltage window, respectively. The energy density and power density of the device are calculated using the following formulas:[45]

$$E = 1/2CV^2 \quad (11)$$

$$P = 3600E/t \quad (12)$$

where E is the energy density (W h kg^{-1}) and P is the power density (W kg^{-1}).

Conclusions

In summary, four samples are obtained by controlling the amount of $Na_2S\cdot 9H_2O$. The best electrochemical performance is obtained with the addition of 1.5 mmol $Na_2S\cdot 9H_2O$. The synthesized samples demonstrate a specific capacity of 1352 F g^{-1} at a current density of 1 A g^{-1}. The capacitance retention remained at 87.82% after 10 000 cycles. The samples form urchin structures after vulcanization, which increase the contact area with the electrolyte. It also promotes the occurrence of redox reactions and ion transport. The $NiCo_2S_4$//AC ASC device provides high energy density at a power density of 2025 W kg^{-1}. These results demonstrate a potential application of $NiCo_2S_4$ sample in energy storage fields and provide a reasonable design approach for highly-efficient electrode material.

Conflicts of interest

The authors declare no conflict of interest.

Acknowledgements

The project was supported by Basic Scientific Research for Universities of Heilongjiang Province (2021-KYYWF-0183).

Notes and references

1 Y. Liu, Y. Liu, X. Wu and Y. R. Cho, *J. Colloid Interface Sci.*, 2022, **628**, 33–40.
2 Y. Liu, Y. Liu and X. Wu, *Chin. Chem. Lett.*, 2023, **34**, 107839.
3 X. L. Jian, H. B. Li, H. Li, Y. X. Li and Y. Y. Shang, *Carbon*, 2021, **172**, 132–137.
4 Z. S. Iro, C. Subramani, J. Rajendran and A. K. Sundramoorthy, *Carbon Lett.*, 2021, **31**, 1145–1153.
5 S. Chen, J. W. Zhu, X. D. Wu, Q. F. Han and X. Wang, *ACS Nano*, 2010, **4**, 2822–2830.
6 Poonam, K. Sharma, A. Arora and S. K. Tripathi, *J. Energy Storage*, 2019, **21**, 801–825.
7 Y. Liu, D. Yan, Y. H. Li, Z. G. Wu, R. F. Zhuo, S. K. Li, J. J. Feng, J. Wang, P. X. Yan and Z. R. Geng, *Electrochim. Acta*, 2014, **117**, 528–533.
8 X. J. Sun, D. D. Zhang, A. Umar and X. Wu, *ACS Appl. Energy Mater.*, 2023, **6**, 9594–9601.
9 H. Q. Liu, M. Z. Dai, D. P. Zhao, X. Wu and B. Wang, *ACS Appl. Energy Mater.*, 2020, **3**, 7004–7010.
10 M. Z. Dai, H. Q. Liu, D. P. Zhao, X. F. Zhu, X. Wu and B. Wang, *ACS Appl. Energy Mater.*, 2021, **4**, 2637–2643.
11 L. F. Shen, J. Wang, G. Y. Xu, H. S. Li, H. Dou and X. G. Zhang, *Adv. Energy Mater.*, 2015, **5**, 1400977.
12 P. Simon and Y. Gogotsi, *Nat. Mater.*, 2008, **7**, 845–854.
13 Z. J. Fan, J. Yan, T. Wei, L. J. Zhi, G. Q. Ning, T. Y. Li and F. Wei, *Adv. Funct. Mater.*, 2011, **21**, 2366–2375.
14 F. Zhao, D. H. Zheng, Y. Liu, F. D. Pan, Q. B. Deng, C. L. Qin, Y. Y. Li and Z. F. Wang, *Chem. Eng. J.*, 2021, **415**, 128871.
15 S. Hasan, A. H. Reaz, S. Das, C. K. Roy and M. A. Basith, *J. Mater. Chem. C*, 2022, **10**, 7980–7996.
16 J. L. Xie, Y. F. Yang, G. Li, H. C. Xia, P. J. Wang, P. H. Sun, X. L. Li, H. R. Cai and J. Xiong, *RSC Adv.*, 2019, **9**, 3041–3049.
17 D. P. Zhao, M. Z. Dai, Y. Zhao, H. Q. Liu, Y. Liu and X. Wu, *Nano Energy*, 2020, **72**, 104715.
18 A. M. Elshahawy, X. Li, H. Zhang, Y. T. Hu, K. H. Ho, C. Guan and J. Wang, *J. Mater. Chem. A*, 2017, **5**, 7494–7506.
19 G. T. Xiang, J. M. Yin, G. M. Qu, P. X. Sun, P. Y. Hou, J. Z. Huang and X. J. Xu, *Inorg. Chem. Front.*, 2019, **6**, 2135–2141.
20 X. J. Chen, D. Chen, X. Y. Guo, R. M. Wang and H. Z. Zhang, *ACS Appl. Mater. Interfaces*, 2017, **9**, 18774–18781.
21 Z. B. Wu, X. L. Pu, X. B. Ji, Y. R. Zhu, M. J. Jing, Q. Y. Chen and F. P. Jiao, *Electrochim. Acta*, 2015, **174**, 238–245.
22 J. Pu, T. T. Wang, H. Y. Wang, Y. Tong, C. C. Lu, W. Kong and Z. H. Wang, *ChemPlusChem*, 2014, **79**, 577–583.
23 S. Hussain, T. M. Liu, N. Aslam, Y. Y. Zhang and S. Q. Zhang, *Mater. Lett.*, 2017, **189**, 21–24.
24 H. Zhang, C. Y. Sun and X. W. Xie, *Electrochim. Acta*, 2023, **466**, 143057.
25 Y. H. Li, H. Liu, J. Xu, Y. Y. Liu, M. R. Wang, J. Li and H. T. Cui, *J. Mater. Chem. A*, 2018, **6**, 19788–19797.
26 M. L. Yan, Y. D. Yao, J. Q. Wen, L. Long, M. L. Kong, G. G. Zhang, X. M. Liao, G. F. Yin and Z. B. Huang, *ACS Appl. Mater. Interfaces*, 2016, **8**, 24525–24535.
27 F. Zhu, H. Xia and T. Feng, *Mater. Technol.*, 2015, **30**, A53–A57.
28 Y. X. Wen, S. L. Peng, Z. L. Wang, J. X. Hao, T. F. Qin, S. Q. Lu, J. C. Zhang, D. Y. He, X. Y. Fan and G. Z. Cao, *J. Mater. Chem. A*, 2017, **5**, 7144–7152.
29 H. C. Chen, J. J. Jiang, L. Zhang, H. Z. Wan, T. Qi and D. D. Xia, *Nanoscale*, 2013, **5**, 8879–8883.
30 J. X. Liu, S. Q. Zhao, A. Umar and X. Wu, *Mater. Today Sustain.*, 2023, **23**, 100433.
31 T. S. Li, Z. F. Zhao, Z. H. Su, S. Y. Lin, R. Sun and Y. C. Shang, *Dalton Trans.*, 2023, **52**, 6823–6830.
32 X. Y. Huai, J. X. Liu and X. Wu, *CrystEngComm*, 2023, **25**, 5310–5315.
33 K. Tao, Y. J. Yang, C. Yang, Q. X. Ma and L. Han, *Dalton Trans.*, 2019, **48**, 14156–14163.

34 L. Yu, L. Zhang, H. B. Wu and X. W. Lou, *Angew. Chem., Int. Ed.*, 2014, **126**, 3785–3788.
35 Y. L. Xiao, Y. Lei, B. Z. Zheng, L. Gu, Y. Y. Wang and D. Xiao, *RSC Adv.*, 2015, **5**, 21604–21613.
36 X. Y. Liu, M. D. Wang, A. Umar and X. Wu, *Dalton Trans.*, 2023, **52**, 10457–10464.
37 X. Y. Liu, M. D. Wang and X. Wu, *Molecules*, 2022, **27**, 7344.
38 T. Chen, L. B. Qiu, Z. B. Yang, Z. B. Cai, J. Ren, H. P. Li, H. J. Lin, X. M. Sun and H. S. Peng, *Angew. Chem., Int. Ed.*, 2012, **51**, 11977–11980.
39 W. Y. Chen, X. M. Zhang, L. E. Mo, Y. S. Zhang, S. H. Chen, X. X. Zhang and L. H. Hu, *Chem. Eng. J.*, 2020, **388**, 124109.
40 T. Tao, X. Han, Q. X. Ma and L. Han, *Dalton Trans.*, 2018, **47**, 3496–3502.
41 Y. Y. Huang, T. L. Shi, S. L. Jiang, S. Y. Cheng, X. X. Tao, Y. Zhong, G. L. Liao and Z. R. Tang, *Sci. Rep.*, 2016, **6**, 38620.
42 G. M. Qu, C. L. Li, P. Y. Hou, G. Zhao, X. Wang, X. L. Zhang and X. J. Xu, *Nanoscale*, 2020, **12**, 4686–4694.
43 L. F. Shen, J. Wang, G. Y. Xu, H. S. Li, H. Dou and X. G. Zhang, *Adv. Energy Mater.*, 2015, **5**, 1400977.
44 X. H. Lu, M. H. Yu, T. Zhai, G. M. Wang, S. L. Xie, T. Y. Liu, C. L. Liang, Y. X. Tong and Y. Li, *Nano Lett.*, 2013, **13**, 2628–2633.
45 J. Rajendran, A. N. Reshetilov and A. K. Sundramoorthy, *RSC Adv.*, 2021, **11**, 3445–3451.